Journal of Materials Chemistry A

ROYAL SOCIETY OF CHEMISTRY

PAPER

View Article Online
View Journal | View Issue

Check for updates

Cite this: J. Mater. Chem. A, 2024, 12, 25254

Regulating electric double-layer dynamics for robust solid-electrolyte interface layer in fast-charging graphite anodes†

Jaeyeon Bang,[a] Seong-Soo Park,[b] Kyungjun Kim,[a] Hwiju Lee,[a] Ilyoung Choi,[c] Youngugk Kim,*[c] JangHyuk Moon *[b] and Sang-Min Lee*[ad]

Received 28th May 2024
Accepted 29th July 2024

DOI: 10.1039/d4ta03703k

rsc.li/materials-a

Graphite is used as an anode material in commercial lithium-ion batteries (LIBs) because of its stable cycling characteristics and high reversibility. However, during fast charging, the deposition of Li metal on the graphite electrode surface becomes problematic because the potential at which Li metal deposition occurs would be close to 0 V (*vs.* Li/Li^+). In this study, we demonstrated an improvement in the fast-charging performance through the effective suppression of Li deposition on the anode surface during fast charging. This was achieved by introducing a metal phosphide nanodot coating layer onto artificial graphite particles. Through various analyses, including density functional theory (DFT) calculations, it was found that the cobalt phosphide(CoP) coating layer increased the concentration of PF_6^- anions in the inner Helmholtz layer (IHL), which in turn induced the formation of an anion-derived solid-electrolyte interface (SEI) layer. A CoP-artificial graphite (AG)/NCM 811 full cell exhibited a high capacity retention (88%) after 300 cycles, without any Li deposition. We also verified the impact of other types of metal phosphides on the fast-charging performance of LIBs. Our findings suggest that the rational design of the SEI layer is feasible through simple surface modifications that induce changes in the properties of the electric double layer. This provides a novel perspective for the design of materials suitable for the rapid charging of LIBs.

1 Introduction

With the growth of the electric vehicle (EV) market, the need for high-performance lithium-ion batteries (LIBs) is increasing. The efficacy of these batteries determines the overall performance of EVs. This has led to significant research efforts aimed at improving their capacity, stability, and charging time.[1–4] The charging time is a particularly crucial parameter that must be addressed to make EVs more popular. Consumers continue to prefer gasoline vehicles because EVs have long charging times. To address this issue, the United States Advanced Battery Consortium (USABC) has set the goal of charging batteries up to 80% within 15 min without a reduction in the energy density or lifespan of the cell.[5–7]

The fast-charging performance of LIBs is primarily determined by the input characteristics of the anode material during electrochemical charging.[8] Graphite, which is currently used as an anode material in commercial LIBs, has the advantages of stable cycling characteristics and high reversibility during charging and discharging. However, because the potential range of the anode at the end of charging is close to the Li deposition voltage, rapid charging causes Li metal deposition on the anode surface.[9–11] The Li metal formed on the anode surface exhibits less reversibility during cycling, leading to capacity loss, and can also cause short circuits due to dendritic formation. This Li deposition occurs because of sluggish reactions at the interface between graphite and the electrolyte relative to the required charging rate.[12,13] During charging, Li ions are inserted into graphite through a sequential process involving Li^+ desolvation, migration (in the solid-electrolyte interface (SEI) layer), and bulk diffusion, where the first two stages present high energy barriers, determining the overall reaction rate.[14] Therefore, during rapid charging, the movement of Li ions approaching the interface occurs faster than the charge transfer, ultimately leading to Li deposition.

To solve this problem, the transport of Li ions at the anode–electrolyte interface must be facilitated.[15–18] In this regard, the formation of a stable SEI layer with a high Li-ion conductivity on the surface of the active material is an effective strategy for

[a]Department of Battery Engineering, Graduate Institute of Ferrous & Eco Materials Technology (GIFT), Pohang University of Science and Technology (POSTECH), 77, Cheonam-Ro, Nam-Gu, Pohang, Gyungbuk 37673, Republic of Korea
[b]Department of Energy Systems Engineering, Chung-Ang University, 84 Heukseok-ro, Dongjak-gu, Seoul 06974, Republic of Korea
[c]Samsung SDI Co., Ltd. R&D Center, Suwon 16678, Republic of Korea
[d]Department of Materials Science and Engineering, Pohang University of Science and Technology (POSTECH), 77, Cheonam-Ro, Nam-Gu, Pohang, Gyungbuk 37673, Republic of Korea

† Electronic supplementary information (ESI) available. See DOI: https://doi.org/10.1039/d4ta03703k

enhancing the movement of Li ions at the graphite-electrolyte interface during fast charging.[12,19–21] Generally, the inorganic components of the SEI layer have a high mechanical strength and low electrical conductivity, which can further suppress electrolyte decomposition.[12,22–25] Among the various inorganic components, LiF is known for its low electronic conductivity, high Li-ion conductivity, and high mechanical strength, which ensure the stability of the SEI layer during cell operation.[26–29] Therefore, the formation of a LiF-rich SEI layer is considered an effective strategy for creating a stable interface during rapid charging and suppressing Li plating.

The formation of the SEI layer on graphite anodes is influenced by the characteristics of the electric double layer (EDL) formed at the electrode–electrolyte interface during initial charging.[30–34] During charging, an electrostatically charged layer of cations and anions is formed on the negatively charged electrode surface, creating an EDL. Subsequently, the decomposition of the cations and anions within the EDL leads to the formation of an SEI layer. By adjusting the distribution of the cations and anions in the EDL, the characteristics of the SEI layer that forms thereafter can be controlled. Generally, LiF is formed by the decomposition of fluorinated components such as $LiPF_6$ or FEC.[24] Hence, to increase the LiF content in the SEI layer, it is necessary to increase the concentration of the fluorinated components in the EDL.

Yang *et al.* introduced potassium methoxide (CH_3OK) as an electrolyte additive to form a LiF-rich SEI layer on the surface of Li metal anodes.[25] The addition of CH_3OK not only promoted the adsorption of anions in the EDL but also influenced the Li^+ solvation structure. Consequently, CH_3O^- diminishes the cation–solvent interaction and enhances the cation–anion interaction, leading to an anion-rich Li^+ solvation structure, which in turn induces the formation of a LiF-rich SEI layer on the Li surface. Sun *et al.* utilized 1.8 M of LiFSI in 1,3-dioxolane as an electrolyte to form a LiF-rich SEI layer on a graphite anode surface.[20] Owing to the high LiFSI concentration, the anion distribution in the EDL increased, resulting in the formation of a LiF-rich SEI layer on the graphite surface. When this electrolyte was used in a graphite half-cell, it demonstrated high capacities of 315 and 180 mA h g^{-1} at 20C and 50C, respectively.

Although the introduction of electrolytes or electrolyte additives to control the formation behavior of the SEI layer is effective, there are limitations in terms of cost and practicality.

For example, when introducing special-purpose electrolyte additives into industry-level full cells, the chemical and electrochemical stabilities of both the anode and cathode must be simultaneously considered. This is because the addition of extra electrolyte additives can lead to increased costs. Moreover, using electrolyte compositions with high salt concentrations can present practical issues in processing, such as low electrolyte impregnation rates, particularly when directly applied to high-loading electrodes; this is a recent major design factor. These issues can also contribute to higher battery costs, hindering practical applications.

In this study, we examined a case in which the composition of the EDL was controlled, and a LiF-rich SEI layer was formed through the surface modification of the active material. The introduction of a cobalt phosphide (CoP) nanodot coating on the surface of artificial graphite (AG) increased the PF_6^- content in the EDL, consequently inducing the formation of a LiF-rich SEI layer. CoP@AG with a LiF-rich SEI layer demonstrated a stable performance without Li plating even after charging at 6C. NCM 811 and CoP@AG full cells exhibited a capacity retention of 85% after 300 cycles under 6C charging/1C discharging conditions and an excellent fast-charging performance, achieving a charge of 80% within 10 min. To elucidate the working mechanism of CoP during SEI layer formation, we analyzed the surface characteristics of the active material with respect to the charging voltage. Through zeta potential and X-ray photoelectron spectroscopy (XPS) analyses, we discovered that the LiCoP phase, formed by the conversion reaction of CoP during charging, altered the charge on the surface of the active material, thereby controlling the EDL behavior. To investigate whether a similar change in the EDL behavior occurs with other types of metal phosphide coatings, we coated iron phosphide (FeP) on the AG surface. We employed various analyses, including density functional theory (DFT) calculations, and discovered that not all metal phosphides facilitate the formation of a LiF-rich SEI layer on particle surfaces. Our study suggests that SEI layer tuning is possible through simple surface modification of the active material, altering the relative ionic distribution within the EDL. Thus, we provide a new perspective in the design of materials suitable for the rapid charging of LIBs.

2 Experimental

2.1 Synthesis of CoP@AG

To synthesize CoP@AG, 0.05 g of Co_3O_4 nanoparticles (Sigma-Aldrich) were initially dispersed in H_2O_2 (30 ml, 35 wt%, Samchun). Once Co_3O_4 was completely dispersed in the solution, 1.25 g of AG (Samsung SDI) was added, and the mixture was stirred for 24 h. The temperature was subsequently increased to 120 °C to fully evaporate the solvent. The resulting Co_3O_4@AG powder was then mixed with NaH_2PO_2 powder (99.9%, Sigma-Aldrich) at a weight ratio of 2 : 1. This mixture was heat-treated at 800 °C in a tube furnace in an Ar gas atmosphere for 2 h at a ramping rate of 5 °C min^{-1}. Finally, the powder was washed in H_2O to remove any residual NaH_2PO_2 and then filtered and vacuum-dried to yield the CoP@AG powder. To synthesize FeP@AG, 0.05 g of Fe_3O_4 nanoparticles (Sigma-Aldrich) were initially dissolved in a mixed solution of H_2O_2 (30 ml, 35 wt%, Samchun) and HNO_3. Subsequently, phosphidation of Fe_3O_4@AG was conducted using the same method as that used for CoP@AG.

2.2 Electrochemical measurement

To evaluate the electrochemical performance, an anode slurry was prepared by mixing an active material (97.5 wt%) with CMC-SBR binder (2.5 wt%) using a Thinky mixer and then coated on a Cu foil (10 μm). The electrodes were vacuum-dried at 100 °C for 10 h. The loading level of the electrode was 6.5 mg cm^{-2}, and the electrode density was set to 1.55 g cm^{-3}. Coin-type half-cells

were assembled in a glove box using graphite electrodes and Li metal. The electrolyte used was 1.15 M $LiPF_6$ in EC/EMC/DMC (3 : 5 : 2 v/v) with 5 wt% FEC. A polypropylene membrane was used as the separator.

To evaluate the characteristics of the SEI layer, 1 M of $LiPF_6$ in EC/DMC of 3 : 7 (v/v) was used to exclude the influence of FEC. An electrochemical evaluation of the fabricated half -cells was conducted using a battery cycler. The formation cycle was repeated twice in the voltage range of 0.01–1.5 V at a rate of 0.1C. Coin-type full cells were fabricated using graphite and NCM811 electrodes. The NCM electrode was prepared by coating a slurry mixed with an active material (95 wt%), Super P (2.5 wt%), and PVDF (2.5 wt%) onto an Al foil. The full cell was designed with an N/P ratio of 1.1. The Gr/NCM full cell underwent three formation cycles at 0.1C, followed by a fast-charging performance evaluation under 6C charging/1C discharging conditions. During the fast-charging capability evaluation, the voltage cut-off for the full cell was set to 4.2 V (charge) and 3 V (discharge).

2.3 Characterization

The morphology, microstructure, and elemental composition of the SEI layer were analyzed using field-emission scanning electron microscopy (FE-SEM, JEOL, JSM-7100F) and field-emission transmission electron microscopy (FE-TEM, JEOL, JEM-2200FS) accompanied by electron energy-loss spectroscopy (EELS). The crystal structures were examined using X-ray diffraction (XRD, D8-Advance Davinci, Bruker). XPS (Nexsa G2, Thermo Fisher) was used to investigate the chemical bonding changes and chemical composition of the SEI layer. To avoid atmospheric exposure, the SEI layer was analyzed in a non-atmospheric open environment. The zeta potential was measured using a Zetasizer (Nano ZS, Malvern Instruments) after dispersing the powder in the electrolyte. The roughness and mechanical strength of the SEI layer were measured using atomic force microscopy (AFM, XE-100, Park Systems).

2.4 Density functional theory calculation

All the DFT calculations were performed using a projector-augmented wave implemented in the Vienna *ab initio* simulation package. The generalized gradient approximation with the Perdew–Burke–Ernzerhof method was used for exchange–correlation functional parameterization. CoP and FeP share the same *Pnma* space group but have different lattice constants. CoP has $a = 5.02$ Å, $b = 3.25$ Å, and $c = 5.50$ Å, whereas FeP has $a = 5.15$ Å, $b = 3.05$ Å, and $c = 5.77$ Å (Fig. S1†).

The LiCoP and LiFeP structures were lithiated by inserting up to 1 mole of Li with the *P*4/*nmm* space group. The LiCoP has $a = 3.64$ Å, $b = 3.64$ Å, and $c = 5.88$ Å, whereas LiFeP has $a = 3.69$ Å $b = 3.69$ Å, and $c = 5.85$ Å (Fig. S2†). The metal-phosphorous surface of CoP and FeP was selected as (200), which is the most energetically favorable surface (Fig. S3†). The graphite (001) surface was selected as a reference to study the adsorption effects of the PF_6^- salt. The cleavage of metal-phosphorus and graphite was modeled using the geometry tool in BIOVIA Material Studio 2021. The PF_6^- salt was relaxed on the cleavage surfaces. The adsorption energies of PF_6^- and various solvents were calculated as follows:

$$E_{ad} = E_{CoP+PF_6^-} - E_{PF_6^-} - E_{CoP}$$

where $E_{CoP+PF_6^-}$, $E_{PF_6^-}$ and E_{CoP} represent the total free energies of adsorbed PF_6^- on the CoP, PF_6^-, and CoP substrates, respectively. The LiF formation energy was calculated using the following equation:

$$E_{LiF} = E_{CoP+F+LiPF_5} - E_{LiPF_5} - E_{CoP} - E_F$$

where $E_{CoP+F+LiPF_5}$, E_{LiPF_5} and $E_F$represent the total free energies of adsorbed $LiPF_6^-$ on the CoP, $LiPF_5$, and fluorine atom respectively. The dissociation of $LiPF_6$ was simulated as a sequential reaction involving the adsorption of PF_6, separation of PF_5 and F, and formation of LiF.

3 Results and discussion

The EDL comprises an inner Helmholtz layer (IHL), an outer Helmholtz layer (OHL), and a diffusion layer. Among these components, the IHL and OHL remain stationary on the particle surface and are unaffected by the flow of the electrolyte.[35] Therefore, the ion distribution in the IHL and OHL during SEI layer formation is crucial because it significantly influences the properties of the SEI layer. Although many studies have demonstrated a correlation between the ion distribution in the EDL and the behavior of the SEI layer formation, most have focused on modifying the EDL components through electrolyte design.[31,36] In this study, we investigated changes in the surface characteristics of artificial graphite through the coating of functional materials, thereby affecting surface potential changes within the EDL. To enhance anion adsorption on artificial graphite surfaces, we modified the surface characteristics of graphite through surface coating. Metal phosphides, known for their excellent catalytic activity, are also promising as anode materials for lithium-ion batteries.[37] Among the various metal phosphides, CoP has been reported to exhibit a high capacity and stable cycling performance when used as an anode material in LIBs.[38] However, its application as a coating material on graphite surfaces remains unexplored. Interestingly, our DFT calculations showed that the anions were adsorbed more strongly on the CoP surface than on the EC solvent (Fig. 1a and S4†). This indicates that CoP facilitates the adsorption of anions, consequently increasing their distribution within the EDL. Conversely, anion adsorption was weaker on the graphite particle surface than on CoP, and the adsorption of the EC solvent was stronger than that of CoP. These results suggest that coating the graphite surface with CoP can significantly enhance anion adsorption within the EDL, potentially altering the SEI layer formation behavior (Fig. 1b and c).

CoP particles were coated on the surface of AG through a two-step reaction process (Fig. 2a). First, crystalline Co_3O_4 particles were coated onto the AG surface using a wet-coating process. Subsequently, the obtained powder was mixed with $Na_2H_2PO_2$ powder, followed by heat treatment at 800 °C to transform the

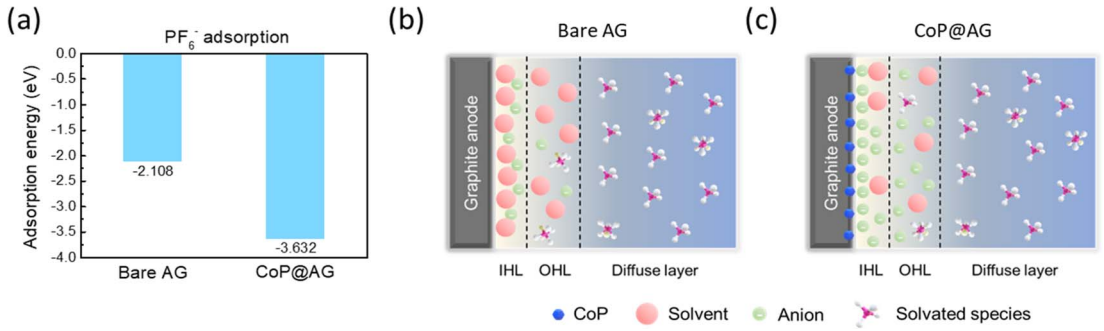

Fig. 1 (a) Adsorption energies of PF_6^- for Bare AG and CoP@AG. Illustration of abundant species in the EDL of (b) Bare AG, (c) CoP@AG.

Co_3O_4 particles into CoP through phosphidation. To verify the crystalline CoP coating, the morphology of AG was observed using FE-SEM and energy dispersive X-ray spectroscopy (EDS) (Fig. 2b–d). Compared with bare artificial graphite (Bare AG), CoP@artificial graphite (CoP@AG) exhibited uniformly distributed nanometer-sized particles on its surface. Through EDS elemental mapping, Co and P signals were detected on the AG surface (Fig. S5†). The amounts of Co and P coated on the

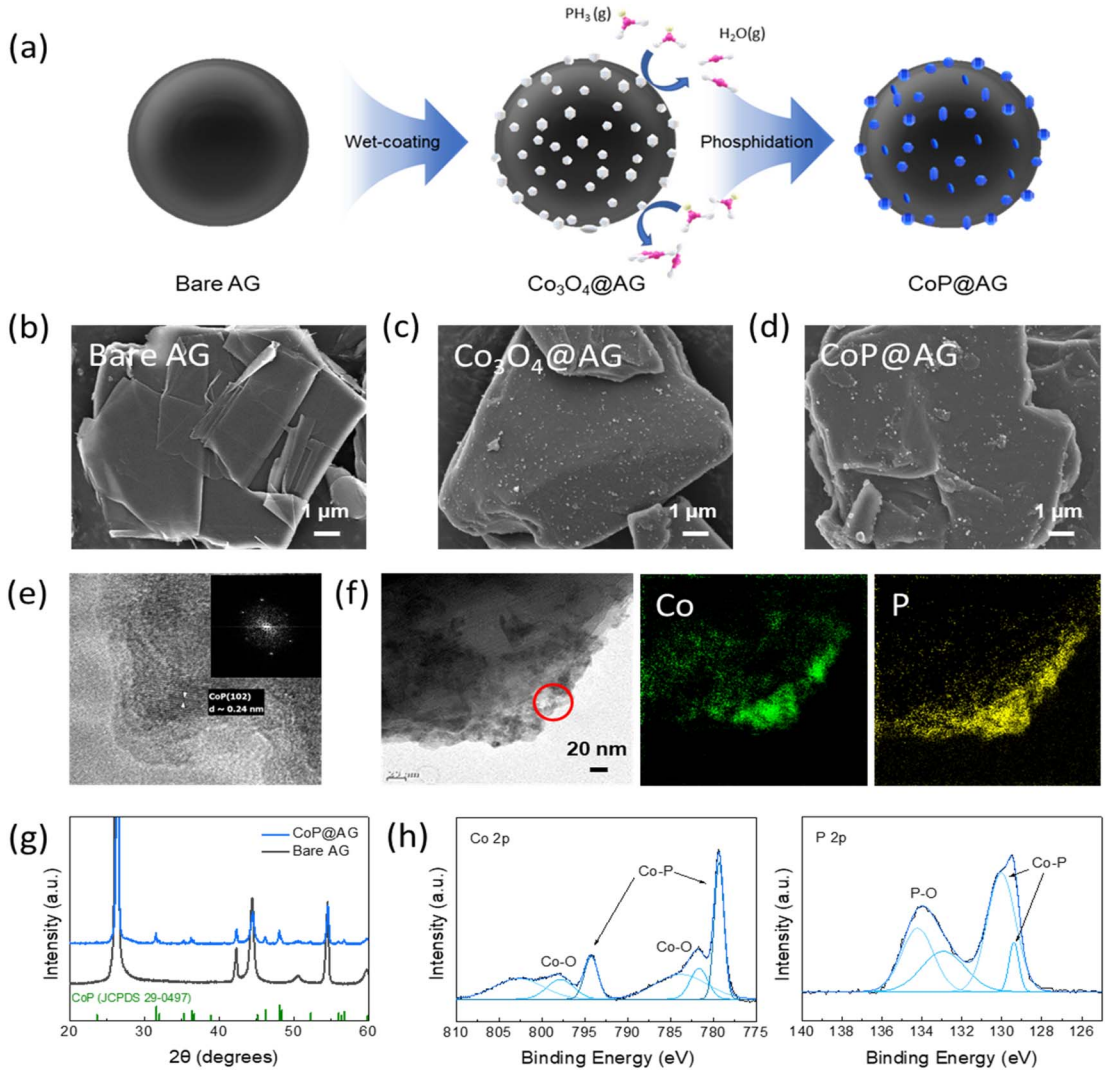

Fig. 2 Material preparation and characterization of CoP@AG: (a) schematic of the CoP@AG preparation process. (b–d) FE-SEM images of Bare AG, Co_3O_4@AG, and CoP@AG. (e) HRTEM images and FFT pattern of CoP@AG. (f) TEM image and EDS elemental mappings of CoP@AG. (g) Powder XRD patterns of Bare AG and CoP@AG. (h) XPS spectra of CoP@AG in the Co 2p (left) and P 2p (right) bands.

surface of artificial graphite were quantified through ICP-OES analysis (Fig. S6†). Through SEM-EDS and ICP analysis, we have confirmed that 0.5 to 0.75 wt% of CoP has been coated on the surface of artificial graphite. A TEM analysis was conducted to ascertain the crystalline state of the coating layer (Fig. 2e and f). High-resolution TEM and fast Fourier transform (FFT) pattern (inset image) analyses confirmed that the particles coated on the graphite surface were crystalline, and an EELS spectrum analysis verified the presence of Co and P in crystalline states. The presence of CoP coated on the surface of artificial graphite was also confirmed through SAED pattern analysis. (Fig. S7†).

An XRD analysis was performed to determine the crystalline structure of the synthesized CoP@AG powder (Fig. 2g). The XRD results indicated that compared with Bare AG, CoP peaks were observed at 32° and 48° in the CoP@AG powder. An XPS analysis was conducted to investigate the surface chemical state of CoP@AG (Fig. 2h). The XPS profiles were deconvoluted based on the C 1s peak at 284.5 eV. In the Co 2p spectrum, Co^{3+} peaks corresponding to CoP were observed at 778 and 794 eV, and in the P 2p spectrum, P^{3-} peaks corresponding to CoP appeared at 129 and 131 eV. From these analytical results, we confirmed the formation of crystalline CoP on the AG surface.

3.1 Structure and formation mechanism of the SEI

To investigate the chemical composition of the SEI, Bare AG and CoP@AG electrodes were analyzed using XPS after the first charge (Fig. 3a and b). An XPS analysis was performed after etching the 2 nm of surface contamination layer with Ar^+ ions. The XPS results for Bare AG, which showed a higher intensity in the C 1s spectrum than CoP@AG, indicated a greater distribution of organic species in the SEI layer of Bare AG. In contrast, the F 1s and Li 1s spectra of CoP@AG exhibited higher LiF intensities, suggesting a prevalent presence of inorganic LiF components in the SEI layer of CoP@AG. In addition, CoP@AG exhibited a lower Li_2CO_3 content. Li_2CO_3 can decompose in a reaction with HF, potentially deteriorating the stability of the SEI layer.[39] These XPS results confirm that the introduction of CoP onto the graphite surface led to the formation of a stable SEI layer.

From the previous analysis of the SEI layer components, we can infer that variations in the inorganic LiF content may influence the mechanical strength of the particle surface.[40] Therefore, to evaluate the effect of the composition of the SEI layer formed after charging on the mechanical properties, we measured the Young's moduli of the Bare AG and CoP@AG electrodes using AFM (Fig. 3c and d). CoP@AG showed

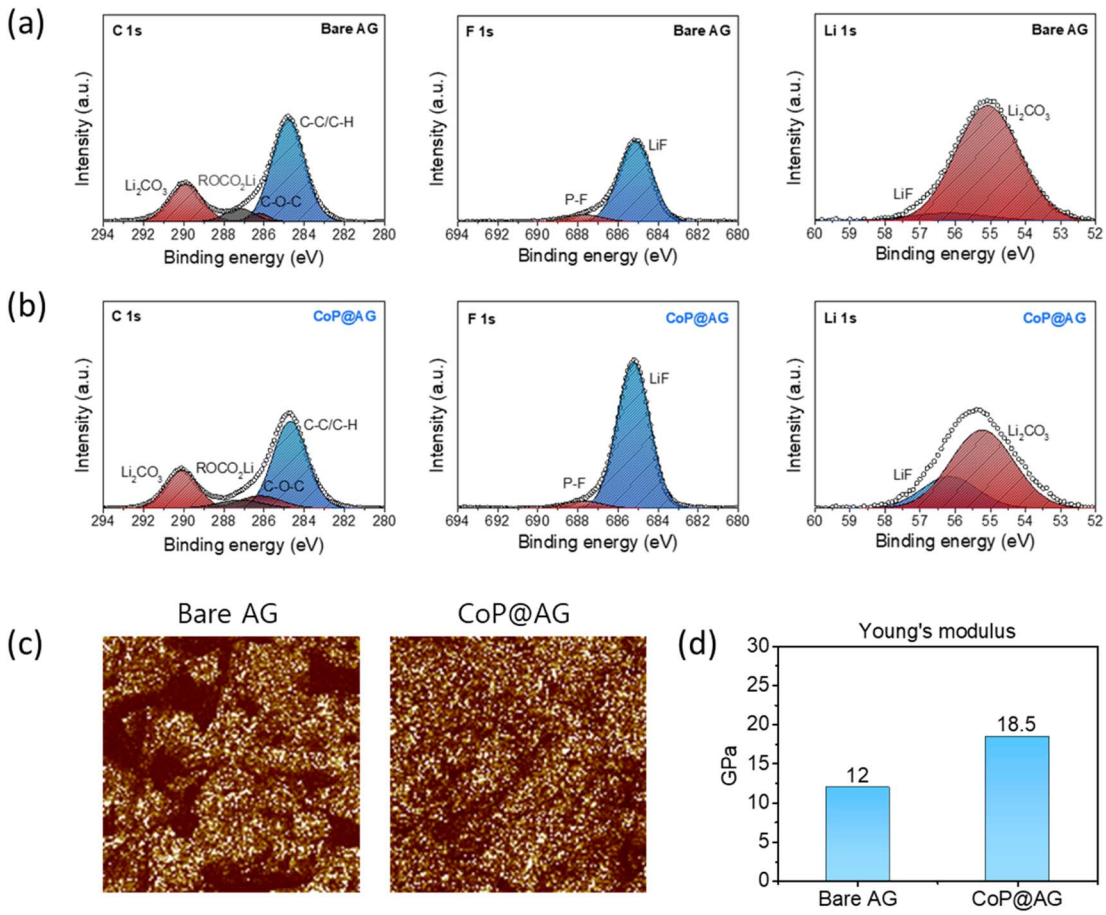

Fig. 3 SEI properties of Bare graphite and CoP@graphite. XPS spectra of Bare graphite (a) and CoP@graphite (b) in the F 1s and Li 1s bands. (c) Young's modulus mapping for Bare AG and CoP@AG electrodes. (d) Bar graph of Young's modulus of Bare AG and CoP@AG.

a uniform Young's modulus mapping and a higher modulus of 18.5 GPa, compared with the uneven mapping and a lower modulus value of 12 GPa for Bare AG, suggesting that the mechanical properties of the SEI layer are enhanced by the increased formation of LiF in the CoP@AG SEI. Moreover, a reduction in the SEI layer resistance was observed after the first charge *via* electrochemical impedance spectroscopy (EIS) (Fig. S8†). These analyses confirm the formation of a LiF-rich SEI layer in CoP@AG.

To explain the formation of LiF predominantly in the SEI layer of CoP@AG after the first charge, we compared the dQ/dV plots from the first cycle charging curves of Bare AG and CoP@AG. We used an electrolyte without the FEC additive for the formation cycle so as to focus solely on the decomposition behavior of the solvent and salt during SEI layer formation (Fig. S9†). During the first charge, Bare AG exhibited a sharp current peak at approximately 0.5 V, which indicates a significant reduction reaction (Fig. 4a).

Typically, in this voltage range, the solvent molecules are reduced and decomposed on the surface of the graphite particles, contributing to the formation of the SEI layer.[41] Thus, for Bare AG, solvent molecules predominantly underwent reduction and decomposition at approximately 0.5 V, resulting in the formation of an organic SEI layer. In contrast, CoP@AG exhibited a smaller and broader reduction current peak at the same voltage. This suggests that the decomposition of the solvent on the surface of the CoP@AG particles was less pronounced than that on Bare AG.

Generally, the formation behavior of the SEI layer varies with the characteristics of the EDL at the electrode–electrolyte interface. Therefore, we hypothesized that the suppression of solvent decomposition on the surface of the CoP@AG particles may have been due to the reduction in the number of solvent molecules in the EDL compared with Bare AG. To examine the changes in the EDL characteristics on the surface of the graphite particles during charging and discharging, the zeta potential was measured. As shown in Fig. 4b, the zeta potentials of the Bare AG and CoP@AG electrodes in their pristine states are similar. However, after charging to 0.01 V, the surface of CoP@AG electrode exhibited a significant negative charge of −7.3 mV (Fig. 4c), reflecting a substantial increase in the anion concentration per unit area in the EDL of CoP@AG after charging. The increase in the anion distribution in the EDL likely facilitated the formation of an anion (PF_6^-)-derived SEI layer on the surface of the CoP@AG particles during the first charge. Therefore, the change in the zeta potential on the surface of the graphite particles suggests a variation in the LiF content of the SEI layers between Bare AG and CoP@AG.

To further investigate the behavior of LiF formation in the SEI layer due to changes in the EDL components, we conducted

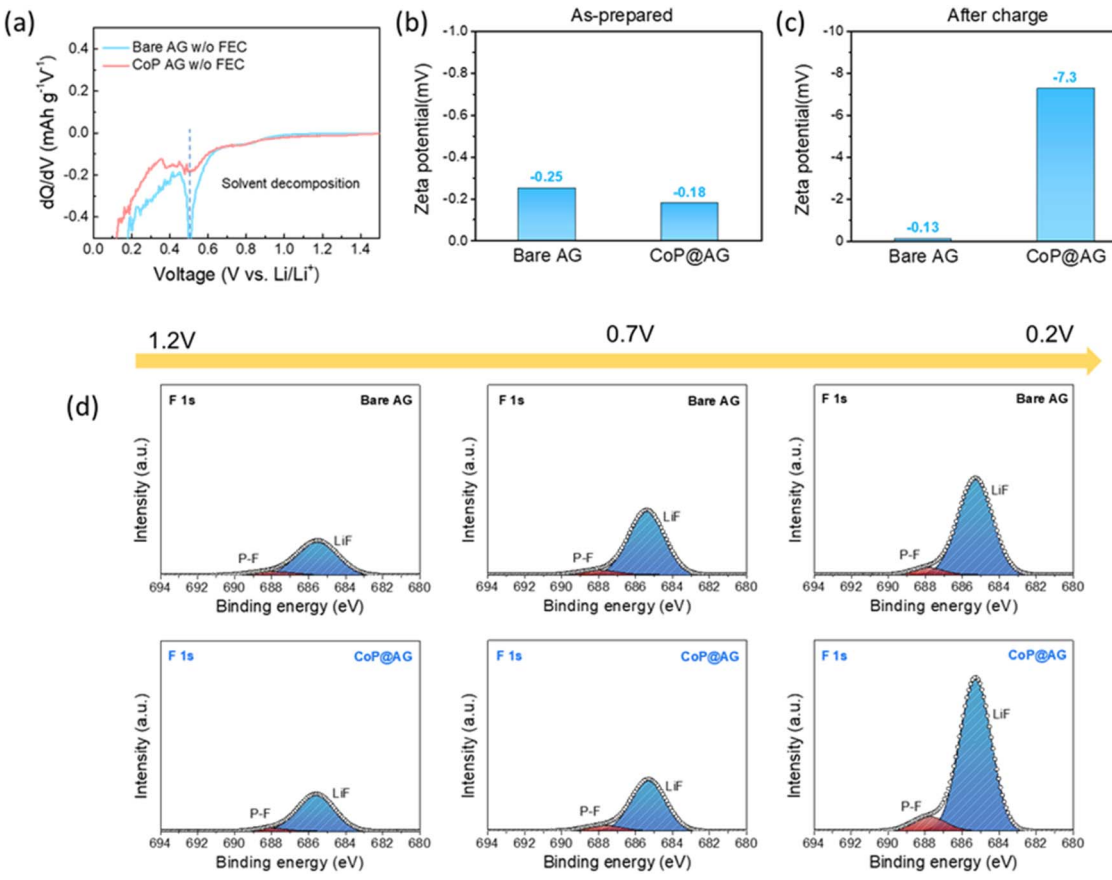

Fig. 4 (a) dQ/dV plots of Bare AG and CoP@AG at 1st lithiation; (b and c) Zeta potential of the pristine/lithiated Bare AG and CoP@AG; (d) SEI compositions of Bare AG and CoP@AG during 1st lithiation.

an XPS analysis of the Bare AG and CoP@AG electrodes after charging at different voltages (Fig. 4d). After charging to 1.2 V and 0.7 V, the intensities of the LiF peak in the SEI layer of both Bare AG and CoP@AG were comparable. However, after charging to 0.2 V, the intensity of the LiF peak in the SEI layer of CoP@AG showed a significant increase compared with that of Bare AG. This indicates a change in the behavior of the EDL on the CoP@AG surface between 0.7 V and 0.2 V, which can be attributed to the chemical changes in the CoP nanoparticles coated on the surface of AG after lithiation.

Prior research has shown that CoP undergoes an intercalation reaction with Li ions at approximately 0.7 V, transforming into LiCoP, and then undergoes a conversion reaction in the voltage range of 0.01–0.12 V, resulting in the formation of Co and Li_3P.[42] Therefore, the increase in the intensity of the LiF peak in the SEI layer of CoP@AG between 0.7 V and 0.2 V can be attributed to the presence of LiCoP, a product of the CoP intercalation reaction.

To elucidate the effect of LiCoP on LiF formation, we performed DFT calculations (Fig. S10†). The adsorption energy of the PF_6^- anion on LiCoP was found to be higher than that on lithiated graphite, suggesting that LiCoP did not enhance the distribution of the PF_6^- anions within the EDL. Based on this finding, we hypothesized that LiCoP primarily facilitates the decomposition of adsorbed PF_6^- into PF_5 and F^-, leading to the subsequent formation of LiF, rather than promoting PF_6^- adsorption itself. The calculations showed that the energy required to decompose PF_6^- into PF_5 and F^- on the surface of LiCoP was lower compared with that on the surface of lithiated graphite. Moreover, the formation energy required for the reaction between decomposed F^- and Li^+ to form LiF was found to be lower on LiCoP than on lithiated graphite. These results confirm that LiCoP enhanced the decomposition of adsorbed PF_6^- and promoted the formation of LiF on the surface, thus predominantly forming LiF within the SEI layer.

To further substantiate the changes in the formation behavior of the SEI layer induced by LiCoP, we compared the SEI layer formation behavior of CoP@AG with that of Co_3O_4 coated on the AG surface, which did not transition through the LiCoP intermediate phase.[43] Similarly to the case of CoP@AG, we examined the evolution behavior of the SEI layer of Co_3O_4@AG through an XPS analysis after charging to 0.7 V and 0.2 V. In the case of Co_3O_4@AG, there was no significant change in the intensity of the LiF peak between 0.7 V and 0.2 V (Fig. S11†). This suggests that the distribution of the solvents/anions within the EDL on the particle surface did not change when coated with a metal oxide that did not undergo the LiCoP phase.

3.2 Fast-charging performance of CoP@AG anode

To evaluate the effect of the LiF-rich SEI on CoP@AG during fast charging, we assessed the electrochemical performance of CoP@AG in a half-cell. In the first cycle, CoP@AG exhibited a slight decrease in the initial coulombic efficiency (ICE) of approximately 2% compared with Bare AG. This is anticipated to have resulted from the conversion reaction of CoP (Fig. S12†). After completing the two-cycle process to ensure the formation of the SEI layer, we assessed the rate capability of the CoP@AG half-cell. Notably, CoP@AG demonstrated a higher constant current (CC) capacity than Bare AG during high-C-rate charging (Fig. S13†).

The fast-charging performance of CoP@AG was subsequently evaluated in a full cell fabricated using NCM811 as the cathode with an N/P ratio of 1.1. The full cell with CoP@AG was fully charged in 22 min, which was 3.3 min faster than that of the Bare AG full cell (Fig. S14†). To verify the suppression effect of Li plating during charging, the cells were charged at 1, 2, 3, and 6C, then disassembled in the lithiated state, and the electrode surfaces were examined using SEM. At charging rates of 1C and 2C, neither Bare AG nor CoP@AG exhibited Li plating, and the particle shapes were clearly visible (Fig. S15†). However, after charging at 3C, Li plating occurred on the Bare AG surface, obscuring the graphite particles, whereas CoP@AG maintained clear graphite particle shapes even after charging at 3C (Fig. 5a). The Li-plating suppression effect of CoP@AG was further confirmed by the voltage profiles. At charging rates of 1C and 2C, at which Li plating did not occur, there was no noticeable difference in the charging curves between the two samples (Fig. 5b and S16†).

However, from 3C, a significant overpotential occurred in the charging curve of Bare AG because of Li plating. In contrast, CoP@AG exhibited a lower overpotential at the same rate, indicating the suppression of Li plating on the electrode surface during rapid charging. This difference in the Li-plating behavior between Bare AG and CoP@AG persisted even after 300 cycles. After 300 cycles of charging at 6C and discharging at 1C, SEM observations of the electrodes in the lithiated state revealed Li dendrites on Bare AG, whereas the graphite particles in the CoP@AG electrodes remained intact without any signs of Li plating (Fig. S17†).

A difference in the rapid-charging performance between Bare AG and CoP@AG was also demonstrated by comparing the CC/CC+CV ratios at each C rate (Fig. S18†). There was no significant difference in the CC charging values between Bare AG and CoP@AG at 1C and 2C. Conversely, a sharp difference in the CC ratio became apparent from 3C, at which Li plating was observed. The suppression of Li plating in the first cycle of rapid charging also influenced the subsequent cycles. After 100 cycles, upon assessing the proportions of CC and CV in the total charging time, CoP@AG was found to have maintained a higher CC charging ratio than did Bare AG (Fig. 5d), indicating that the Li-plating suppression effect of CoP@AG continued to be effective over multiple cycles.

After confirming the differences in the Li-plating behavior between Bare AG and CoP@AG during the first cycle of rapid charging, we evaluated the long-term cycle stability of CoP@AG in a full cell under fast-charging conditions (Fig. 5e). After 100 cycles, the capacity of Bare AG significantly decreased, showing a capacity retention of 74%. In contrast, CoP@AG demonstrated a stable cycling behavior under rapid-charging conditions, maintaining a capacity retention of 89% after 100 cycles (Fig. 5d and S19†). The lower capacity retention of Bare AG compared with that of CoP@AG can also be explained by the differences in

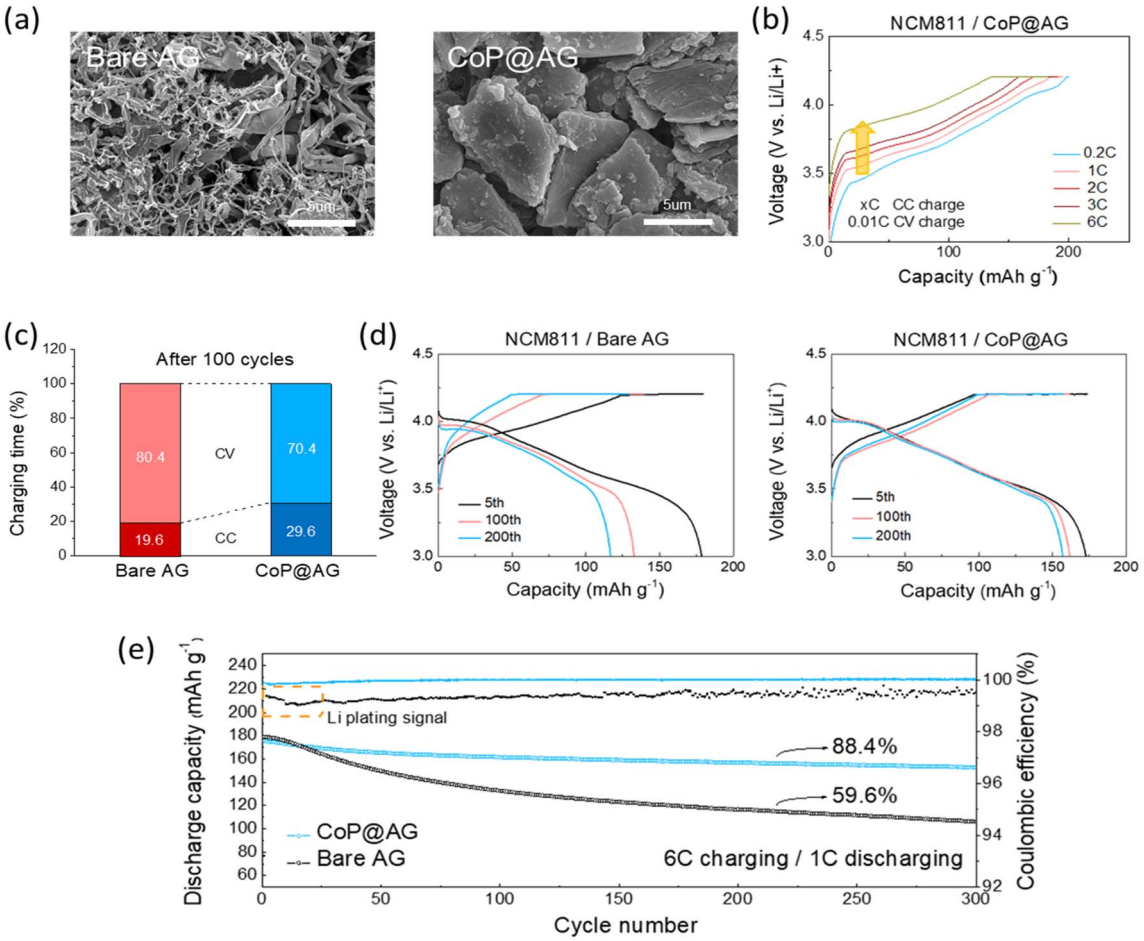

Fig. 5 (a) SEM top-view images of Bare AG and CoP@AG electrode after 3C charge, (b) voltage profile of CoP@AG electrode at various C rates, (c) relative contributions of CC and CV charging modes to the total charging time after 100 cycles, (d) voltage profiles of full cells assembled with Bare AG and 0.5 wt% CoP@AG anodes at selected cycles, (e) capacity decay and CEs of full cells with Bare AG and CoP@AG anodes. Cycling was performed at charge/discharge rates of 6C/1C.

the coulombic efficiency over the cycles (Fig. 5e). In the first 20 cycles, the coulombic efficiency of Bare AG rapidly decreased owing to the reduced charging capacity caused by Li plating. In contrast, the CoP@AG full cell consistently exhibited a high coulombic efficiency (~99.8%) from the first cycle. Owing to the low coulombic efficiency resulting from Li plating, Bare AG exhibited a capacity retention of only ~59% after 300 cycles, whereas CoP@AG effectively suppressed Li plating, achieving a high capacity retention of ~88%. ESI Table 1† compares the fast-charging performance of the CoP@AG anode developed in this work with those of various anode materials reported in the literature and clearly demonstrates a significant improvement in the fast-charge cyclability of LIBs achieved in this study.

3.3 Verification of universality

We discovered that CoP formed a LiF-rich SEI layer on the graphite surface. To investigate whether a similar change in the EDL behavior occurs with other types of metal phosphide coatings, we coated FeP onto the AG surface. Iron phosphide, which has a reaction mechanism similar to CoP, has been reported to undergo an intercalation reaction to form LiFeP phases, suggesting potential changes in the EDL due to this reaction.[44] To reveal the characteristics of the EDL when FeP is coated on the graphite surface, we assessed the solvent/anion adsorption preference of FeP using DFT calculations (Fig. 6a). Similar to CoP, FeP also exhibited a lower adsorption energy for PF_6^- than for graphite. However, unlike LiCoP, LiFeP required

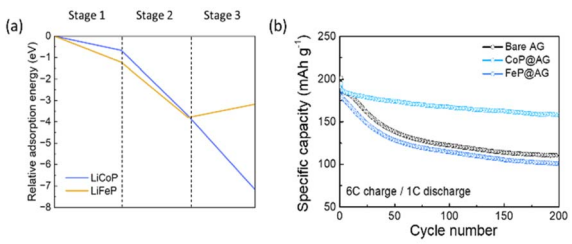

Fig. 6 (a) Relative adsorption (formation) energies of PF_6^- adsorption (Stage 2), PF_6^- decomposition (Stage 3), and LiF formation (Stage 3) on LiCoP and LiFeP surfaces. (b) Capacity decay of full cells with Bare AG, CoP@AG, and FeP@AG anodes. Cycling was performed at charge/discharge rates of 6C/1C.

a high formation energy for the reaction to convert decomposed PF_5 and F^- into LiF. This indicates that the formation of LiF in the SEI layer due to FeP was less effective than that due to CoP.

To experimentally validate the DFT calculations, we examined the SEI layer formation behavior of FeP@AG using XPS (Fig. S20†). To compare this behavior with that of CoP@AG, we charged the cells to the same voltage, obtained the electrodes, and analyzed the SEI layer components on the electrode surface using XPS. In the F 1s spectrum, FeP@AG, unlike CoP@AG, did not show a significant change in the intensity of the LiF peak between 0.7 V and 0.2 V. This indicates that LiFeP, formed by the intercalation reaction between Li and FeP, does not facilitate the formation of a LiF-rich SEI layer. The variation in the SEI layer components between CoP@AG and FeP@AG also affected the fast-charging performance (Fig. 6b and S21†). In a full cell test under 6C charge/1C discharge conditions, FeP@AG showed a lower capacity retention compared with the superior performance of CoP@AG. This indicates that Li plating occurred during rapid charging as the SEI layer in FeP@AG did not form a LiF-rich layer.

DFT calculations and XPS results revealed that not all metal phosphides can promote the formation of a LiF-rich SEI layer on particle surfaces. Furthermore, electrochemical evaluations confirmed that the fast-charging performance of FeP@AG does not improve compared with that of Bare AG. These findings offer insights into the design of more efficient materials for LIBs incorporated with metal phosphides as the anode material.

4 Conclusion

We formed a LiF-rich SEI layer on the surface of graphite particles to suppress Li plating on the graphite anode surface during fast charging. To induce a LiF-rich SEI, we coated the graphite surface with CoP, which increased the anion distribution in the EDL, as confirmed by the DFT calculations and zeta potential analysis. CoP@AG with a LiF-rich SEI layer demonstrated a stable performance without Li plating, even after rapid charging. NCM 811 and CoP@AG full cells exhibited a capacity retention of 88% after 300 cycles under 6C/1C charge/discharge conditions and an excellent fast-charging performance, achieving a charge of 80% within 10 min. Moreover, we analyzed the surface characteristics of the active material based on the charging voltage to elucidate the working mechanism of CoP during SEI layer formation. Through zeta potential and XPS analyses, we found that the LiCoP phase formed by the intercalation reaction of CoP during charging altered the charge on the surface of the active material, thereby controlling the distribution of the anions/solvent in the EDL. To investigate whether a similar change in the EDL behavior occurs with other types of metal phosphide coatings, we coated FeP onto the AG surface. Our analyses revealed that not all metal phosphides facilitate LiF-rich SEI layer formation on particle surfaces.

Our study suggests that SEI layer tuning is possible through a simple surface modification of the active material, altering the ionic composition within the EDL. Thus, we provide a new perspective in the design of materials for the fast charging of LIBs.

Author contributions

Jaeyeon Bang: conceptualization, methodology, investigation, writing – original draft; Seongsoo Park: DFT analysis and writing – original draft; Kyungjun Kim, Hwiju Lee, Ilyoung Choi: resources; Youngugk Kim (corresponding author): supervision; JangHyuk Moon (corresponding author): conceptualization, supervision; Sang-Min Lee (corresponding author): conceptualization, writing – review & editing, funding acquisition and supervision.

Data availiability

The data supporting this article have been included as part of the ESI.†

Conflicts of interest

There are no conflicts of interest to declare.

Acknowledgements

This research was supported by the Korea Institute for Advancement of Technology (KIAT) grant funded by the Korean Government (MOTIE) (P0012748, HRD Program for Industrial Innovation). This research was also supported by Samsung SDI.

Notes and references

1 D. Larcher and J. M. Tarascon, *Nat. Chem.*, 2015, **7**, 19–29.
2 D. A. Notter, M. Gauch, R. Widmer, P. Wager, A. Stamp, R. Zah and H. J. Althaus, *Environ. Sci. Technol.*, 2010, **44**, 6550–6556.
3 P. G. Balakrishnan, R. Ramesh and T. P. Kumar, *J. Power Sources*, 2006, **155**, 401–414.
4 V. Etacheri, R. Marom, R. Elazari, G. Salitra and D. Aurbach, *Energy Environ. Sci.*, 2011, **4**, 3243–3262.
5 J. Neubauer, A. Pesaran, C. Bae, R. Elder and B. Cunningham, *J. Power Sources*, 2014, **271**, 614–621.
6 K. J. Zhao, M. Pharr, J. J. Vlassak and Z. G. Suo, *J. Appl. Phys.*, 2010, **108**, 073517.
7 Y. Y. Liu, Y. Y. Zhu and Y. Cui, *Nat. Energy*, 2019, **4**, 540–550.
8 S. S. Zhang, *J. Power Sources*, 2006, **161**, 1385–1391.
9 Y. C. Chang, J. H. Jong and G. T. K. Fey, *J. Electrochem. Soc.*, 2000, **147**, 2033–2038.
10 A. Satoh, N. Takami and T. Ohsaki, *Solid State Ionics*, 1995, **80**, 291–298.
11 Y. O. Kim and S. M. Park, *J. Electrochem. Soc.*, 2001, **148**, A194–A199.
12 E. Kazyak, K. H. Chen, Y. X. Chen, T. H. Cho and N. P. Dasgupta, *Adv. Energy Mater.*, 2022, **12**, 2102618.
13 J. W. Lee, S. Y. Kim, D. Y. Rhee, S. Park, J. Y. Jung and M. S. Park, *ACS Appl. Mater. Interfaces*, 2022, **14**(26), 29797–29805.
14 K. Xu, A. von Cresce and U. Lee, *Langmuir*, 2010, **26**, 11538–11543.

15 S. Ahmed, I. Bloom, A. N. Jansen, T. Tanim, E. J. Dufek, A. Pesaran, A. Burnham, R. B. Carlson, F. Dias, K. Hardy, M. Keyser, C. Kreuzer, A. Markel, A. Meintz, C. Michelbacher, M. Mohanpurkar, P. A. Nelson, D. C. Robertson, D. Scoffield, M. Shirk, T. Stephens, R. Vijayagopal and J. C. Zhang, *J. Power Sources*, 2017, **367**, 250–262.

16 T. Abe, F. Sagane, M. Ohtsuka, Y. Iriyama and Z. Ogumi, *J. Electrochem. Soc.*, 2005, **152**, A2151–A2154.

17 K. Persson, V. A. Sethuraman, L. J. Hardwick, Y. Hinuma, Y. S. Meng, A. van der Ven, V. Srinivasan, R. Kostecki and G. Ceder, *J. Phys. Chem. Lett.*, 2010, **1**, 1176–1180.

18 T. Baba, K. Sodeyama, Y. Kawamura and Y. Tateyama, *Phys. Chem. Chem. Phys.*, 2020, **22**, 10764–10774.

19 M. Baek, J. Kim, J. Jin and J. W. Choi, *Nat. Commun.*, 2021, **12**, 6807.

20 C. C. Sun, X. Ji, S. T. Weng, R. H. Li, X. T. Huang, C. N. Zhu, X. Z. Xiao, T. Deng, L. W. Fan, L. X. Chen, X. F. Wang, C. S. Wang and X. L. Fan, *Adv. Mater.*, 2022, **34**(43), 2206020.

21 S. B. Tu, B. Zhang, Y. Zhang, Z. H. Chen, X. C. Wang, R. M. Zhan, Y. T. Ou, W. Y. Wang, X. R. Liu, X. R. Duan, L. Wang and Y. M. Sun, *Nat. Energy*, 2023, **8**(12), 1365–1374.

22 J. Chen, X. L. Fan, Q. Li, H. B. Yang, M. R. Khoshi, Y. B. Xu, S. Hwang, L. Chen, X. Ji, C. Y. Yang, H. X. He, C. M. Wang, E. Garfunkel, D. Su, O. Borodin and C. S. Wang, *Nat. Energy*, 2020, **5**, 386–397.

23 N. Qin, L. M. Jin, Y. Y. Lu, Q. Wu, J. S. Zheng, C. M. Zhang, Z. H. Chen and J. P. Zheng, *Adv. Energy Mater.*, 2022, **12**, 2103402.

24 J. Tan, J. Matz, P. Dong, J. F. Shen and M. X. Ye, *Adv. Energy Mater.*, 2021, **11**, 2100046.

25 J. L. Yang, M. H. Li, Z. J. Sun, X. Lian, Y. A. Wang, Y. X. Niu, C. L. Jiang, Y. N. Luo, Y. Liu, Z. L. Tian, Y. Long, K. Zhang, P. C. Yu, J. Zhang, Z. H. Wang, G. Wu, M. Gu and W. Chen, *Energy Environ. Sci.*, 2023, **16**, 3837–3846.

26 Z. J. Ju, C. B. Jin, X. H. Cai, O. W. Sheng, J. C. Wang, J. M. Luo, H. D. Yuan, G. X. Lu, X. Y. Tao and Z. Liang, *ACS Energy Lett.*, 2022, **8**, 486–493.

27 X. Q. Zhang, X. B. Cheng, X. Chen, C. Yan and Q. Zhang, *Adv. Funct. Mater.*, 2017, **27**, 1605989.

28 W. Huang, H. Wang, D. T. Boyle, Y. Z. Li and Y. Cui, *ACS Energy Lett.*, 2020, **5**, 1128–1135.

29 R. Pathak, K. Chen, A. Gurung, K. M. Reza, B. Bahrami, J. Pokharel, A. Baniya, W. He, F. Wu, Y. Zhou, K. Xu and Q. Qiao, *Nat. Commun.*, 2020, **11**, 93.

30 R. Xu, X. Shen, X. X. Ma, C. Yan, X. Q. Zhang, X. Chen, J. F. Ding and J. Q. Huang, *Angew. Chem., Int. Ed.*, 2021, **60**, 4215–4220.

31 C. Yan, H. R. Li, X. Chen, X. Q. Zhang, X. B. Cheng, R. Xu, J. Q. Huang and Q. Zhang, *J. Am. Chem. Soc.*, 2019, **141**, 9422–9429.

32 C. Y. Yang, J. Chen, T. T. Qing, X. L. Fan, W. Sun, A. von Cresce, M. S. Ding, O. Borodin, J. Vatamanu, M. A. Schroeder, N. Eidson, C. S. Wang and K. Xu, *Joule*, 2017, **1**, 122–132.

33 Y. F. Zhou, M. Su, X. F. Yu, Y. Y. Zhang, J. G. Wang, X. D. Ren, R. G. Cao, W. Xu, D. R. Baer, Y. G. Du, O. Borodin, Y. T. Wang, X. L. Wang, K. Xu, Z. J. Xu, C. M. Wang and Z. H. Zhu, *Nat. Nanotechnol.*, 2020, **15**, 224–230.

34 Q. S. Wu, M. T. McDowell and Y. Qi, *J. Am. Chem. Soc.*, 2023, **145**, 2473–2484.

35 C. Yan, R. Xu, Y. Xiao, J. F. Ding, L. Xu, B. Q. Li and J. Q. Huang, *Adv. Funct. Mater.*, 2020, **30**, 1909887.

36 M. L. Mao, X. Ji, Q. Y. Wang, Z. J. Lin, M. Y. Li, T. Liu, C. L. Wang, Y. S. Hu, H. Li, X. J. Huang, L. Q. Chen and L. M. Suo, *Nat. Commun.*, 2023, **14**, 1082.

37 S. M. Lee, J. Kim, J. Moon, K. N. Jung, J. H. Kim, G. J. Park, J. H. Choi, D. Y. Rhee, J. S. Kim, J. W. Lee and M. S. Park, *Nat. Commun.*, 2021, **12**, 39.

38 Z. L. Liu, S. J. Yang, B. X. Sun, X. H. Chang, J. Zheng and X. G. Li, *Angew. Chem., Int. Ed.*, 2018, **57**, 10187–10191.

39 A. T. S. Freiberg, J. Sicklinger, S. Solchenbach and H. A. Gasteiger, *Electrochim. Acta*, 2020, **346**, 136271.

40 S. Chen, L. L. Huang, X. Y. Wen, Q. R. Chen, Z. Y. Xia, S. L. Li, H. Wang, M. Q. Xu and W. S. Li, *J. Phys. Chem. C*, 2023, **127**, 11462–11471.

41 M. Y. Nie, J. Demeaux, B. T. Young, D. R. Heskett, Y. J. Chen, A. Bose, J. C. Woicik and B. L. Lucht, *J. Electrochem. Soc.*, 2015, **162**, A7008–A7014.

42 Z. Y. Zhou, X. R. Shi, J. P. Yin, W. Q. Kong, J. C. Sun and Z. S. Wen, *Chem. Phys. Lett.*, 2020, **749**, 137403.

43 Q. Guo, Q. Ru, B. Wang, Y. D. Mo, Z. Wang, P. Zhang, X. H. Hou and S. J. Hu, *J. Alloys Compd.*, 2017, **728**, 910–916.

44 S. Boyanov, J. Bernardi, F. Gillot, L. Dupont, M. Womes, J. M. Tarascon, L. Monconduit and M. L. Doublet, *Chem. Mater.*, 2006, **18**, 3531–3538.